01 Jan 2022

On the Effect of Hot Rolling on Inclusion Size and Distribution in a Cast AISI 1070 Steel Railroad Wheel

Jacob M. Summers

Soumava Chakraborty

Laura Bartlett
Missouri University of Science and Technology, lnmkvf@mst.edu

Ronald J. O'Malley
Missouri University of Science and Technology, omalleyr@mst.edu

et. al. For a complete list of authors, see *https://scholarsmine.mst.edu/matsci_eng_facwork/2906*

Recommended Citation

ON THE EFFECT OF HOT ROLLING ON INCLUSION SIZE AND DISTRIBUTION IN A CAST AISI 1070 STEEL RAILROAD WHEEL

Jacob M. Summers , **Soumava Chakraborty, Laura N. Bartlett, Ronald J. O'Malley and Mario F. Buchely**
Department of Metallurgical Engineering, Missouri University of Science and Technology, Rolla, MO 65409, USA

Richard Pilon
Amsted Rail Company, Overland Park, KS, USA

Abstract

The goal of this work is to examine the effect of hot deformation on shrinkage porosity and nonmetallic inclusions in an AISI 1070 grade steel industrially produced wheel casting. Steel cleanliness is an important consideration as it influences the mechanical properties of the final product. A high density of porosity and inclusions have been shown to be detrimental for mechanical properties, especially during hot rolling. Using a laboratory-scale rolling mill, cast preforms were subjected to a 66% cumulative reduction to determine the effect of thermomechanical processing on void closure and inclusions that may produce anisotropy in mechanical properties. Quantitative automated feature analysis, AFA, of inclusion type, size, morphology, and distribution was conducted utilizing an Aspex PICA 1020 scanning electron microscope to determine differences in inclusions and shrinkage porosity in the as-cast and as-rolled conditions. The results were compared with previously reported impact toughness values which indicated a trend with MnS projected length and average impact toughness in the T-L orientation. Reduction in shrinkage porosity was also verified utilizing 3D micro-X-ray CT scans. The AFA results showed a decrease in shrinkage porosity from 177 ppm in the as-cast condition to less than 35 ppm after rolling. Pores were in general much smaller and widely distributed after hot rolling and this would suggest improved impact properties. Analysis of nonmetallic inclusions revealed three primary categories of inclusions that included MnS, Al_2O_3, and complex inclusions that mainly consisted of MnS with an Al_2O_3 core, with small quantities of mixed silicates of Mn and Al and calcium aluminates ($CaAl_2O_4$).

Keywords: SEM AFA, micro-X-ray CT scans, void closure, impact toughness, hypoeutectoid steel, inclusion analysis, projected length

Introduction

Inclusions and shrinkage porosity have previously been associated with rail failures and have been reported by the American Railway Engineering Association (AREA) Committee on Rails in numerous AREA Bulletins as early as 1947.[1] Porosity has been shown by Hardin and Beckermann to reduce the elastic modulus during tensile testing of an AISI 8630 steel and was measured by radiography.[2] A drop from 200 to 150 GPa was noted with a difference of 0.2 porosity fraction determined by radiographic analysis.

Hot rolling has been shown by a variety of researchers to induce porosity closure due to the plastic compressive strain. Higher temperatures have been shown to close porosity more effectively through ease of welding of the matrix.[3] In a study by Ganguly et al.,[4] Johnson–Cook parameters were determined and applied for material flow predictions during plane strain hot rolling which were utilized to predict the effects of different rolling parameters on void closure. For the same reduction ratio, temperature was directly proportional to increases in equivalent plastic strain from 0.3 at 1100 °C to 0.45 at 1300 °C for the same pass in the rolling schedule. These modeling results are in agreement with experimental testing and modeling performed by Kukuryk.[5]

Dhua et al. investigated the effect of nonmetallic inclusions (NMI) on mechanical properties for commercial heats of pearlitic steel for application to the railway industry. Their work primarily focused on examining the effects of NMI on fracture toughness (K_{IQ}) and high-cycle fatigue limit. Reducing the volume fraction of inclusions from 0.45 wt. % to less than 0.19 wt. % increased fracture toughness, K_{IQ} from 42.33 to 49.88 MPa$\sqrt{}$m. Increasing steel cleanliness also resulted in an increase in the fatigue limit from 319 to 355 MPa.[6] Grigorovich et al. examined mechanical properties across multiple rail producers in Europe and Asia and concluded that the volume fraction of coarse NMI could be used to characterize the sensitivity of the metal to contact-fatigue-crack nucleation.[7] They showed the relationship between volume fraction of brittle oxide inclusions and their size correlated strongly with service durability particularly with inclusions larger than 8 μm. It is well known that aspect ratio of NMI effects mechanical properties and that hot rolling can cause elongated NMI which are detrimental for impact toughness.[8] This is generally correlated to overall sulfur content although at sufficiently low levels the sulfur content are less impactful as shown in a study of a 0.3 wt. % C, Ni-Mo-Cr steel which had an anisotropy ratio, defined as the longitudinal toughness over the transverse toughness, of 3.5 for all hot-rolled steel samples with sulfur contents in the range of 0.005 to 0.017 wt. %.[8] Hot working effects brittle and plastic inclusions differently and can introduce directionality into the inclusion population. The aspect ratio of plastic inclusions is most significantly affected by hot rolling which was correlated with upper shelf energies of a low-carbon steel which detailed the detrimental effect of elongated plastic inclusions on toughness.[9]

While nonmetallic inclusions (NMIs) are inevitable as a result of the steel refining and casting process, it is necessary to examine their effect on final microstructure and attempt to minimize the detrimental effects on mechanical properties. Sulfide and oxy-sulfides have inherent morphology related to the deoxidation practice and include Type I, Type II, Type III, and Type IV. Deoxidation practices involve Al to bind with O and produce Al_2O_3 influencing the morphology of sulfide inclusions. Type I morphology is produced by incomplete deoxidation resulting in random large globules with high residual O. If there is high residual Al content from deoxidation and low O, large angular and random, Type III formation is favored. If complete deoxidation is achieved, there is low residual Al content and low O content favoring intergranular fine Type II sulfides.[11] Type II MnS has been shown to be detrimental for toughness.[12] Type IV is a modified globular morphology typically achieved through rare earth additions or calcium treatment. Therefore, this morphology is usually achieved as a part of inclusion engineering to form favorable inclusion morphology with desirable Al and O contents. It is well established in literature that hot worked NMI such as MnS results in anisotropic properties relating

to decreases in transverse properties such as ductility, fatigue life, and impact toughness.[13] In this work, the deoxidation practice leads to very low dissolve Al content (~20 ppm) and low O (~30 ppm) leading to Type II being the expected morphology of sulfide inclusions. However hot working is desirable to break down macrosegregation, minimize shrinkage porosity, and refine the grain structure of cast products.

In the casting process for train wheels, it is not traditionally possible to hot roll the material, and the traditional wheel rolling process in a forging line would not induce ample deformation to significantly alter mechanical properties. However, through the use of cast preforms subjected to a modified wheel rolling mill introduces greater localized deformation, such as in the web and rim section of the wheel, resulting in localized dynamic recrystallization (DRX) and location specific mechanical property improvement through refinement of grain size. Understanding the effect of a simulated rolling process on NMI and porosity will ensure the industrial process is viable and determine what level of impurity is allowable without excess anisotropy. Therefore, in an attempt to optimize mechanical properties for a high-carbon steel through hot rolling, the NMI aspect ratio will be examined to determine if there is a correlation with aspect ratio and anisotropy for previous experimental work. The goal of this work is to ascertain if any discontinuities such as shrinkage porosity and NMI have an effect on fracture in the investigated rail steels. This work will investigate the influence of isothermal rolling temperature on nonmetallic inclusions for a high-carbon 1070 steel and the relationship between NMI and anisotropy (Figure 1).
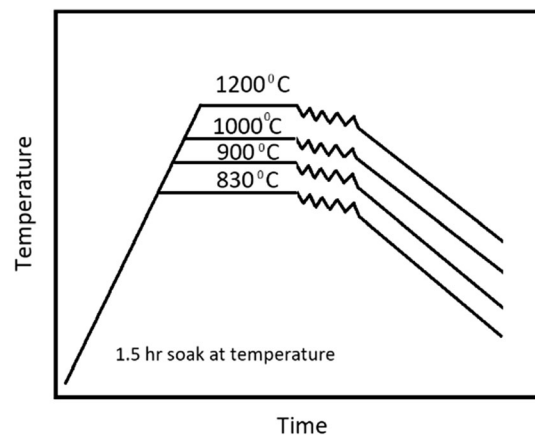

Figure 1. The steel casting was soaked in an electric box furnace with SiC elements for 1.5 hrs at the process temperature before hot rolling and subsequent slow cooling (~0.1s⁻¹) in a refractory blanket.

Procedure

The steel in question was cast industrially and sectioned for examination. The average composition of the samples is given in Table 1. Samples were taken from 1400 lb castings produced in an electric arc furnace (EAF) ($\sim$20 tons of steel). Ferrosilicon and ferromanganese were added to the ladle prior to tapping to deoxidize the melt. Prior to tapping, a small amount of Al was added to scavenge the remaining oxygen to fully kill the steel (Figure 2). The steel is cast from the ladle into semi-permanent graphite molds using pressure pouring technology resulting in castings with a columnar, dendritic solidification of the castings due to the high thermal gradient. The proposed process will involve a mold design which allows for oversize web and rim area which will be subjected to localized deformation through the use of a modified wheel rolling mill traditionally used in a forging line. To simulate this process in a laboratory setting, isothermal hot rolling trials were conducted for an AISI 1070 steel at a 66% cumulative reduction. The location for analysis with respect to the industrially cast railway blank is shown in Figure 3 which is sectioned to include the centerline segregation region. Charpy specimens with standard U-notch tested at 20 °C were prepared for analysis (Figure 2) with the samples being sectioned directly below ($\sim$2 to 3 mm) the fracture surface. As a short summary of the treatment condition, samples were held for 1.5 hours at temperature to allow uniform heating and then were hot-rolled from an initial thickness of $\sim$43.5 mm to $\sim$14.5 mm as described in Figure 1 and then prepared for Charpy testing by ASTM E23. One sample was prepared at each temperature with three Charpy samples investigated in each orientation and averaged to report their average notch toughness.

The L-S and T-L orientations were prepared for automated feature analysis (AFA) to analyze porosity and NMI and their effect on anisotropy in previous experimental results. Fracture surfaces were removed from Charpy specimens after testing at 20 °C, and the surface beneath was polished to 0.1 μm. AFA was performed on an Aspex scanning electron microscope (SEM) with an accelerating voltage of 20 kV. Two scans were combined for each flat polish surfaces, one focused on micro porosity and shrinkage porosity and the other for NMI. To ensure that the results are representative of the sample, Aspex PICA-1020 (Particle Identification and Characterization Analyzer) is utilized displayed in Figure 4. During this analysis, a region is

selected and broken down into multiple fields selected for analysis at random (Figure 4a,b). The fields are selected at random and broken down into nine smaller fields (Figure 4c) which are then systematically analyzed for differences in contrast from the metal matrix flagging in the system that an inclusion or pore is present (Figure 4d). The center of such a feature is identified, and EDS analysis is performed quickly to collect chemistry information of the particles for later classification along with measurement of diameter and area of each feature. A large number of inclusions for an effective comparison are obtained through Aspex PICA-1020 (3,527-4,082 dependent on number density). The stitch scan is performed at a magnification of 1000x for the inclusion analysis and 200x for the porosity analysis to ensure proper measurement of more coarse pores.

Along with AFA, degree of porosity closure was also investigated through micro-X-ray CT scans of the as-cast and as-rolled 1000 °C material using a Xradia 510 Versa X-ray microscope. A stitched scan method was employed
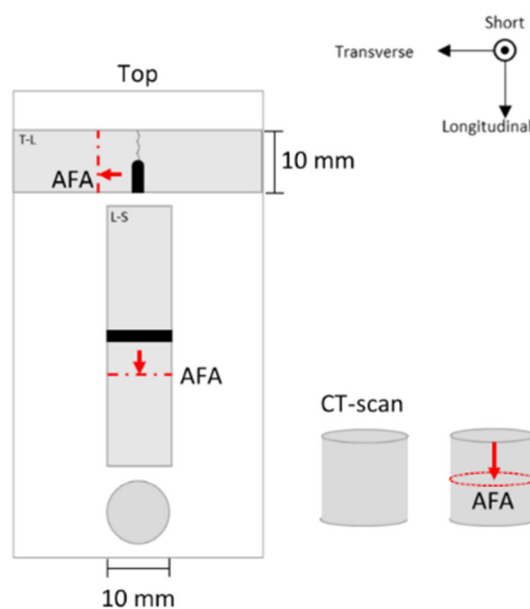

Figure 2. Aspex PICA-1020 performed in a stitched scan for shrinkage porosity and NMIs. Charpy specimens were prepared below the fracture surface for L-S and T-L samples, and the CT scan sample (10x10 mm cylinder) was removed from the as-cast and as-rolled 1000 °C sample.

Table 1. Composition of the AISI 1070 As-Cast Steel in Weight Percent

C*	Si	Mn	Cu	Cr	Mo	Ni	P	S*	Nb	Al	Ti	Fe
0.706	0.53	0.73	0.168	0.13	0.025	0.048	0.004	0.021	0.004	0.002	0.0008	Bal.

*Concentrations of sulfur and carbon were determined utilizing LECO combustometric analysis
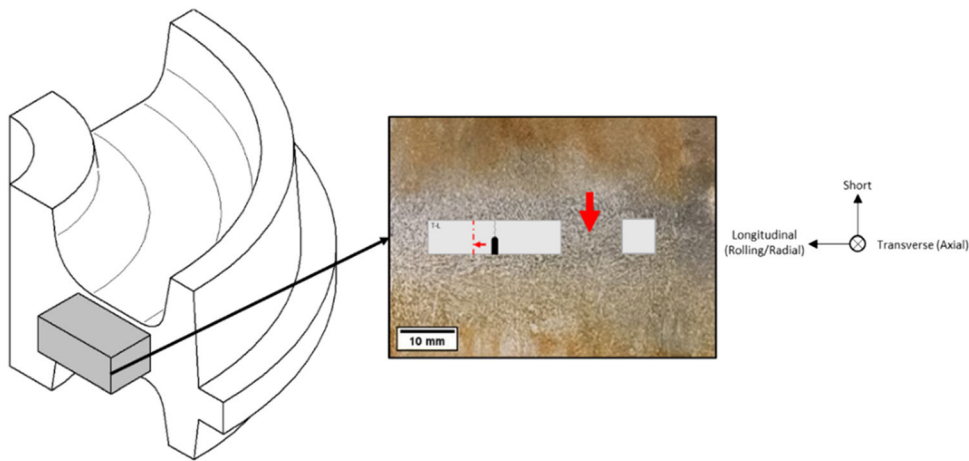
Figure 3. The location of the rolled samples as well as the sampling location is in the equiaxed region including the centerline segregation region for the as-cast and as-rolled samples.
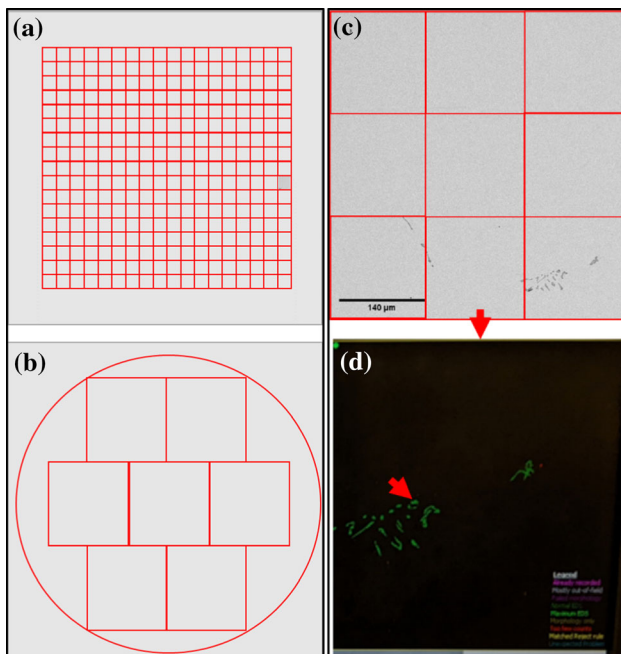

Figure 4. Aspex PICA-1020 performed in a stitched scan for shrinkage porosity and NMIs. The scan regions at 1000x for NMIs (a) and 200x for shrinkage porosity (b). A single field of the NMI scan is displayed in (c) which is split into 9 regions that are analyzed systematically for size, distribution, and chemistry (d).

where an initial scan was run at 160 V and a second at 140 V, and the two were overlayed to minimize artifacts and enhance the ability to post-process the samples. The CT results were processed into slices of ~ 10.66 μm which were then thresholded manually in Matlab, converted to a stack in Fiji, and rendered in a 3D volume using the 3D viewer plugin. Particles were also measured in terms of volume and mean radius using the 3D Object Counter tool in Fiji. In the AFA and CT scan, the particle information is obtained relating to the size and amount of the particles

related to the overall scanned region which were analyzed and compared. Finally, to better understand the interaction between NMIs and shrinkage porosity on fracture in the as-cast and as-rolled samples, the fracture surfaces from the L-S and T-L orientation were sectioned in half to reveal a cross section of the fracture surface and examine the relationship between the matrix and the primary crack as shown in Figure 5. Samples were polished to 0.05-μm finish and etched with 4% Picral and then examined in the Tescan Vega3 scanning electron microscope (SEM) using an accelerating voltage of 20 kV. Backscatter electron (BSE) and secondary electron (SE) images were captured of relevant features.

Results and Discussion

AFA Porosity Results

The AFA results for the porosity scan are plotted in Figure 6. The average diameter pore size for all conditions is concentrated in the 5 to 40 μm range. The as-cast condition has the largest area fraction of pores greater than 5 μm at 160 ppm. The high content of coarse porosity indicates centerline shrinkage is present in the as-cast condition. The amount of porosity in each as-rolled condition that is an average size between 5 and 40 μm is less than 34 ppm and decreases as the rolling temperature is increased. This indicates a significant reduction in shrinkage porosity at all temperatures. From 900 to 1200 °C, there is also an apparent decrease from 34 to less than 1 ppm of porosity in the size range of 5 and 40 μm providing some evidence of temperature dependence. Porosity between 2 and 5 μm in diameter is also reduced in the as-rolled conditions from 12 ppm in the as-cast to less than 3 ppm at all rolling temperatures. In the as-cast condition, the area fraction of pores larger than 40 μm was 21 ppm.
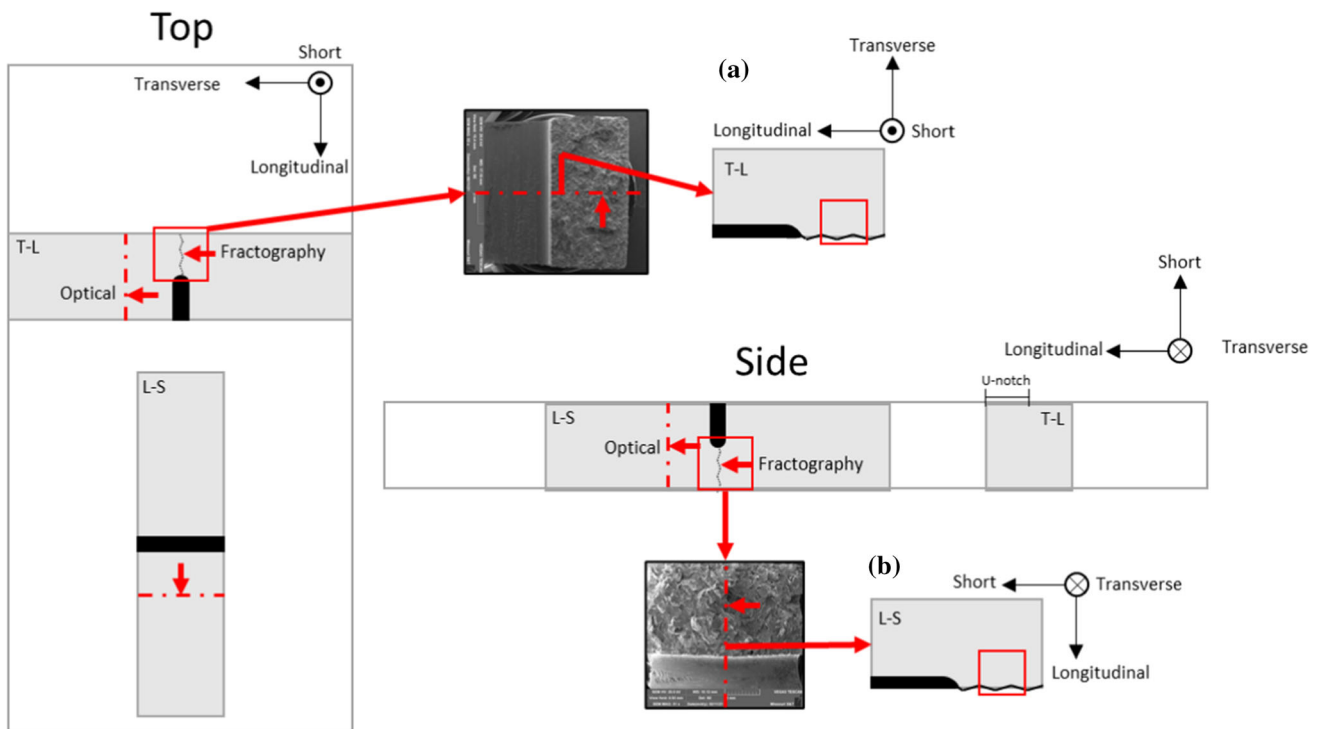
Figure 5. *Depiction of the sectioning method used to prepare cross sections of fracture area to determine NMI and shrinkage porosity interaction with the primary crack. Etched with 4% Picral and the red box indicates the location for comparative BSE images. T-L (a) and L-S (b) are shown with relevant coordinate systems where the rolling direction and longitudinal are synonymous. Fracture surfaces in the chart are the as-cast segregate region sample at 20 °C and as-rolled 830 °C at a 66% cumulative reduction in the T-L orientation tested at 20 °C.*
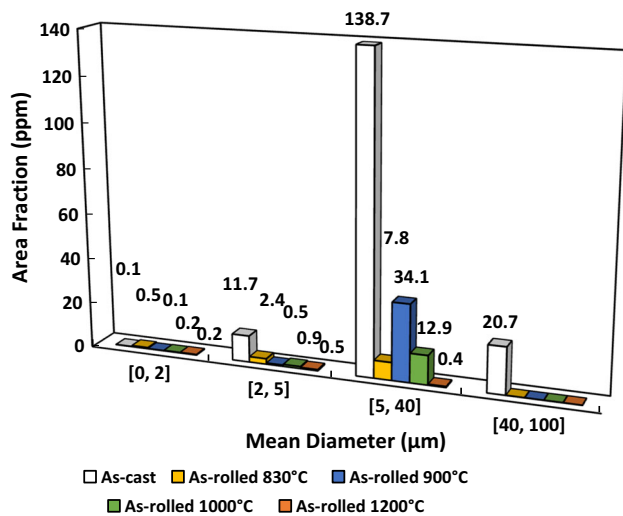

Figure 6. *Area fraction (ppm) versus average pore diameter (μm) in the as-cast and as-rolled conditions. No pores measured greater than 100 μm.*

Table 2. *Nearest-Neighbor Distance Calculation for the Particles in Each Porosity Scan*

Condition	Average NND (μm)	Standard deviation (μm)
As-cast	219.3	248.8
As-rolled 830 °C	542.3	421.5
As-rolled 900 °C	712.7	825.8
As-rolled 1000 °C	817.4	599.0
As-rolled 1200 °C	1245.6	709.3

Along with size, the nearest-neighbor distance (NND) quantifies the distance between pores serving as an indicator of the likelihood to participate in crack initiation. The results of the NND calculation for each sample are shown in Table 2. NND was quantified by isolating the porosity observed in each scan and measuring their relative position to their nearest-neighbor pore. The first observable trend is very high standard deviation. The spacing between pores varies across the sample surfaces in the AFA scans with some regions having little to no porosity. Therefore, porosity is not uniformly distributed in the cast or rolled conditions. The increase in standard deviation with average NND could indicate that the porosity content is lowered through hot rolling but the size comparison in Figure 6 is a better indication of the porosity closure at different rolling temperatures. Overall, the results still indicate that greater porosity closure was experienced at 1200 °C which agrees with the results from Ganguly et al.[4].
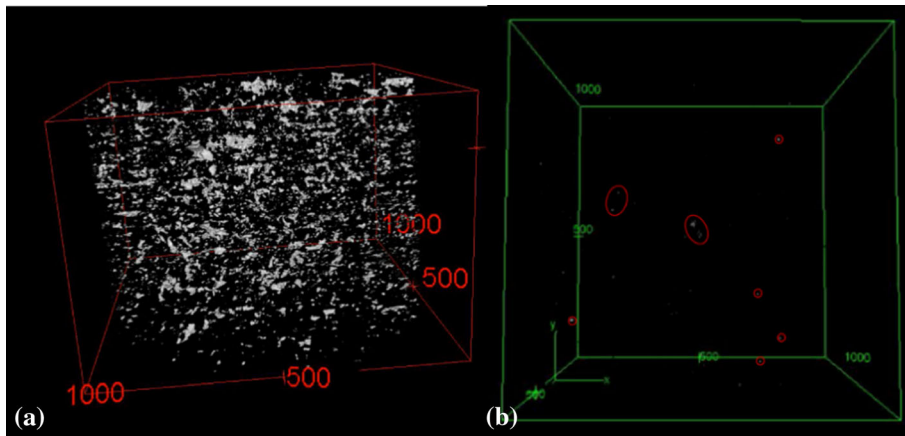
Figure 7. CT scans of the as-cast (a) and as-rolled 1000 °C (b) sample which visualizes the degree of closure of porosity at a 66% cumulative reduction.

To verify the results of the Aspex PICA-1020 and determine a more time efficient method for determining shrinkage porosity content, the as-cast and as-rolled 1000 °C sample was sectioned for micro-X-ray CT analysis. The results of scanning a 10 × 10 mm cylinder are shown in Figure 7. A qualitative comparison of the as-cast (Figure 7a) and as-rolled 1000 °C (Figure 7b) shows that the large shrinkage porosity present in the as-cast condition is largely closed at a 66% cumulative reduction at 1000 °C which agrees with the Aspex AFA results.

A central slice with a height of 3.2 mm was investigated separately using the 3D Objects Counter in Fiji to determine the volume, surface area, centroid, and mean radius of each pore as shown in Figure 8. The sample is rendered three dimensional for the as-cast sample (Figure 8a) and as-rolled 1000 °C (Figure 8c) with the central cross section displayed in Figure 8b and d for the as-cast and as-rolled 1000 °C sample, respectively. Red arrows indicate the thresholded porosity analyzed. By taking the relationship between mean volume and mean diameter in the analysis of this region, relationships in a log-log plot between the volume and diameter were used to estimate the volume from the cross section analyzed in the automated feature analysis for comparison. Additional information on these calculations can be found in Appendix I.

The calculated volume for the as-cast and as-rolled 1000 °C condition is compared to the average volume from the CT scan results along with a comparison of the average diameter of the shrinkage porosity in Table 3. The mean diameter and mean volume reflect the same relationship between the automated feature analysis and the CT scans. The scanned region in the automated feature analysis represents an area with smaller pores than that represented in the CT scans. This is expected due to the variation in
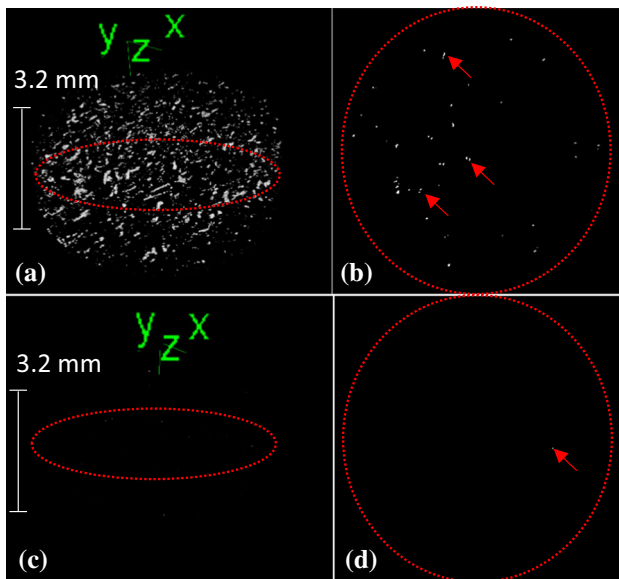

Figure 8. Central region (3.2 mm height) of the micro-X-ray CT scans in the as-cast (a,b) and as-rolled 1000 °C (c,d) conditions. The red dotted line (a,c) represents the central cross section of each sample which is isolated for the as-cast (b) and as-rolled 1000 °C (d) condition. Each individual particle thresholded had the volume, surface area, centroid, and mean radius calculated using the 3D Objects Counter in Fiji.

Table 3. Summary of the Aspex PICA-1020 and Micro-X-ray CT Scans Results Including Mean Diameter (μm) and Volume (μm³) × 10⁵

Condition	Mean Diameter (μm)		Mean volume (μm³) × 10⁵	
	Aspex PICA-1020	CT-scan	Aspex PICA-1020	CT-scan
As-cast	6.4	49.8	0.07	1.74
As-rolled 1000 °C	4.3	24.2	0.03	0.18

apparent shrinkage porosity content throughout the cast sample. The smallest pore measured in both samples had a mean diameter of 16 μm which explains the inconsistencies between the automated feature analysis and the CT scans. The automated feature analysis has a resolution of 0.5 μm as the minimum size. Therefore, combining the techniques is possible for verifying the closure of shrinkage porosity but not that of micro-voids. However, micro-voids less than eight microns are not expected to be as detrimental to mechanical properties. Area and volume fraction in ppm reported by mean pore size is plotted in Figure 9 to compare the results of the automated feature analysis and CT scans further. It is of note that 92 to 93% of the porosity in the as-cast condition and as-rolled 1000 °C is comprised of porosity larger than 5 μm. The peak porosity size shifts in the as-cast condition when comparing the automated feature analysis and CT scan results.

With a larger sample volume, it is likely that the peak shift to shrinkage porosity in the 40 to 100 μm is likely more representative of shrinkage porosity size than that of the cross section investigated through automated feature analysis. To further support this result, the cross section of the as-cast CT scan sample was re-polished until shrinkage porosity was present on the surface. This feature was examined optically as shown in Figure 10 and processed in Fiji for mean diameter. The formula obtained for the as-cast diameter–volume relationship in the central slice was applied to estimate the mean volume of these features and can be seen tabulated in Table 4 (see Appendix 1 for additional information). This validates the existence of large shrinkage porosity in the CT scans. Because this feature was not represented in the AFA, it is likely that the mean diameter and estimated mean volume for the as-cast

condition are not as accurate. To improve the estimate, future work could involve mounting the full CT scan sample, polishing to 12 iterative depths, and performing automated feature analysis on each region. Reducing the diameter of the investigated sample for CT scans could also improve the resolution down to 8 μm ($\sim$7 mm diameter sample) to ensure sufficient closure of detrimental voids. The time to perform the analysis of the central slice of the CT scan using the 3D Object Counter allows for analysis of 300 regions per sample in 30 minutes, whereas the AFA scan of 1 region per sample takes approximately 6 hours. Therefore while the results of the automated feature analysis and CT scan are difficult to correlate, the micro-X-ray CT scan does provide a cost-effective and time-effective technique for investigating shrinkage porosity closure during hot rolling. It also indicates that hot rolling at a 66% reduction at 1000 °C closed $\sim$98% of the shrinkage porosity with a mean diameter greater than 156 μm with the AFA extending the analysis to micro-voids down to 0.5 μm indicating that $\sim$92% of the total porosity was closed at 1000 °C.

AFA Inclusion Results

Inclusions were examined as a function of thermomechanical processing utilizing backscattered scanning electron microscopy with energy-dispersive X-ray spectroscopy (EDS). The most prominent inclusions are MnS, Al_2O_3, and complex inclusions of MnS and Al_2O_3. Figure 11 displays the Type II MnS inclusions found in the as-cast material. The spectrograph shows the peaks for Mn and S along with trace amounts of C and N. Type II inclusions are the primary morphology of MnS in this steel which is expected with the fully killed deoxidation practice with a residual content of 20 ppm Al which has been shown to be detrimental to toughness[9]. This is important because hot rolling alters both the equilibrium microstructure and the spacing and aspect ratio of deformable nonmetallic inclusions like MnS. Al_2O_3 is also seen in the cast structure as a small cluster as seen in Figure 12. The spectrograph shows a peak of Al and O as expected but also a small amount of Mn. The significance is that proper classification of NMI requires careful examination of the ternary phase diagram of primary inclusion compositions and determining, along with verification from the images, what peak should be considered "trace." Al_2O_3 inclusions are classified based on their Al content in the absence of scanning for O during AFA. Complex inclusions are also common in this steel which are a mixture of MnS and Al_2O_3 as seen in Figure 13. The MnS is seen surrounding the Al_2O_3 inclusion which occurs due to preferential formation on the clusters which also typically maintain a round morphology, although a rodlike and round complex inclusion are seen in Figure 13. The peak for the MnS spectrograph of the inclusion has Mn and S peaks as expected with a well-established Al peak. This is also true when examining the
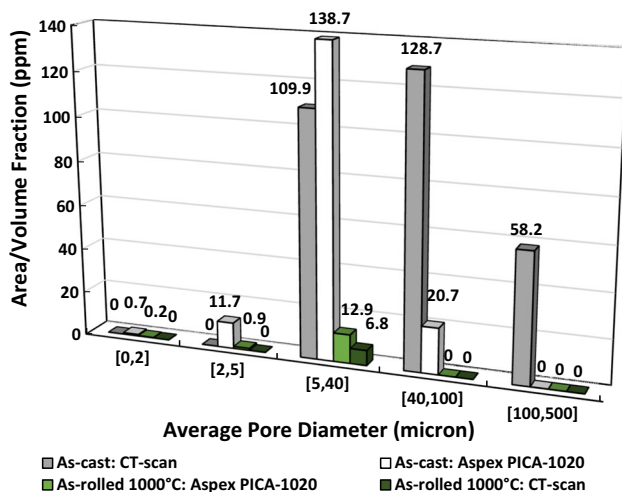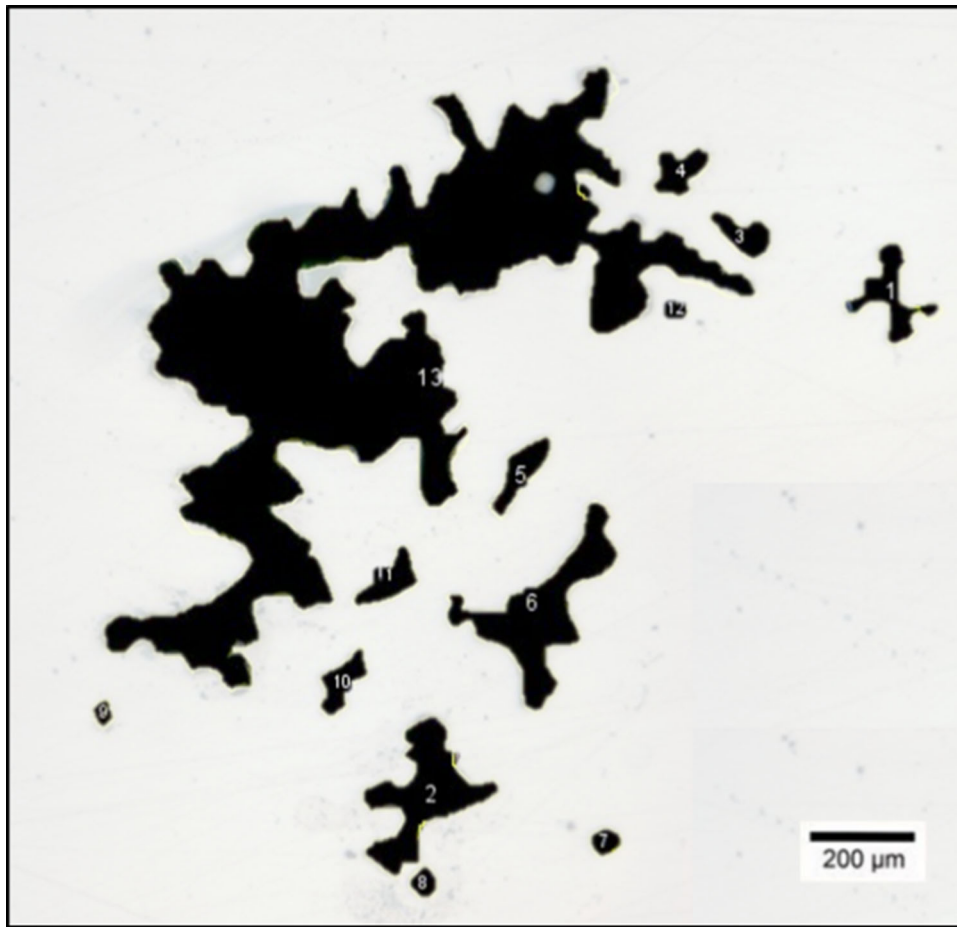

Figure 9. Area/volume fraction (ppm) of the as-cast and as-rolled 1000 °C samples. The Aspex PICA-1020 and CT scan methods are compared. From single cross sections, the automated feature analysis results seem to misrepresent the presence of shrinkage porosity for the as-cast condition.

Figure 10. Optical microscopy of large shrinkage porosity (~1500 μm).

Table 4. Image Analysis of Mean Diameter (μm) and Mean Volume (μm³) × 10⁵

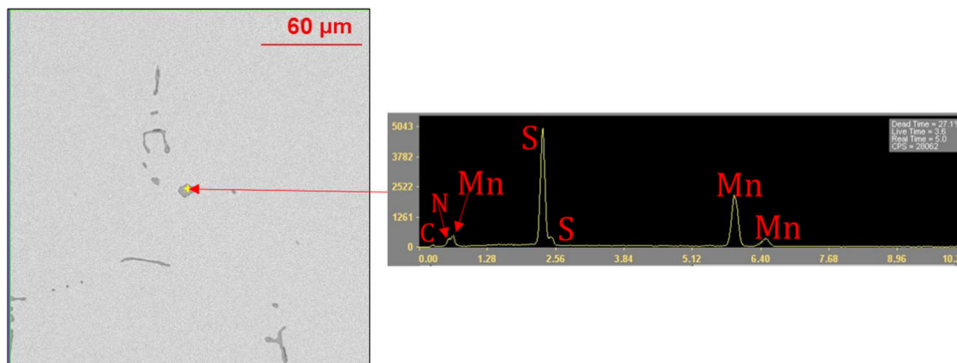| Condition	Mean diameter (μm) Optical sample	Mean volume (μm³) × 10⁵ Optical sample
As-cast	261.6	927.3

Figure 11. EDS spectrum of MnS inclusions. Type II and III MnS in as-cast material with 210 ppm S and residual Al from deoxidation of around 20 ppm.
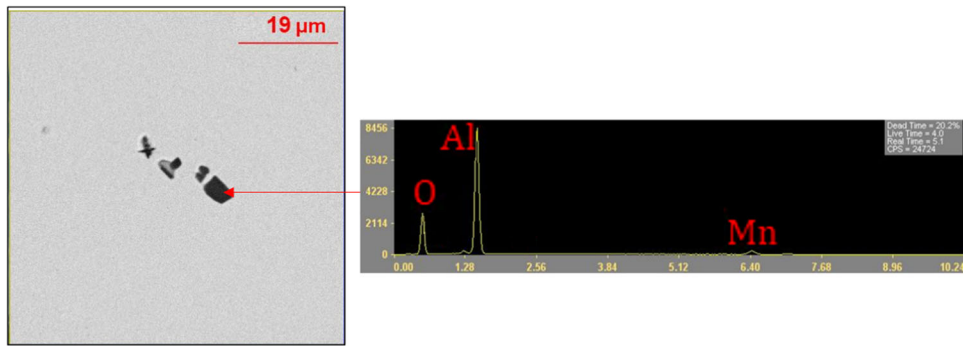
Figure 12. EDS spectrum of Al₂O₃ cluster. Al₂O₃ cluster in the as-cast material of a small enough size that it did not float out prior to solidification and became entrained in the metal as an inclusion.
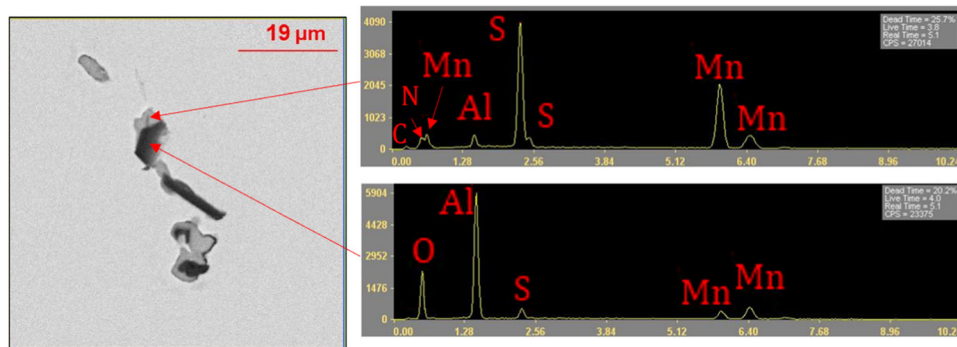

Figure 13. EDS spectrum of globular complex inclusion of Al2O3 and MnS inclusions.

Al_2O_3 spectrograph which has Al and O peaks and discernible Mn peaks. The MnS acts as a shell for the Al_2O_3 inclusions, and therefore when the center of a complex inclusion is measured, the EDS map also includes the peaks from both Al_2O_3 and MnS phases making the classification discernible from pure Al_2O_3 or pure MnS inclusions.

To represent the particles in each condition, the raw results from the AFA were plotted in joint-ternary diagrams which were used to determine classifications of the inclusions. The as-cast condition is shown in the L-S orientation in Figure 14a and the T-L orientation in Figure 14b. The as-rolled 830 and 1200 °C AFA scans are represented in Figure 14c–f with 900 and 1000 °C in the T-L represented in Figure 15. The primary elements related to inclusions in this system are Mn, S, and Al, coming from Al-killing with trace amounts of Al to combine with O, Si, and trace amounts of Ca and Mg from contamination during casting from treatment and furnace refractory. The average diameter of each inclusion is organized by size in the ranges of 0 to 40 μm. To represent the size of inclusions present in each condition, the percentage of each size range is displayed in a pie chart. The L-S orientation for the as-cast sample shows a fine microstructure with 81% particles less than 2 μm, but T-L orientation has only 62% particles less than 2 μm with 36% being between 2 and 5 μm, and 1% is between 5 and 40 μm. The as-rolled 830 °C has 81% fine

particles less than 2 μm in the L-S orientation and 78% in the T-L orientation with the number of coarse particles between 5 and 40 μm increased to 1%. At 1200 °C, the L-S orientation has 85% fine particles less than 2 μm and 87% fine particles in the T-L orientation with 0% coarse particles above 5 μm indicating a variance in the overall size of inclusions. Even 1% of coarse particles can pose issues for mechanical properties. Figure 15 includes the T-L orientation of the 900 and 1000 °C samples which both have fairly fine inclusions with 87% less than 2 μm in average diameter.

The Mn-Al-S field and Mn-S-Si fields contain a large portion of the particles and were the focus when identifying the classifications of the NMIs. Based on these fields, classification for MnS, Al_2O_3, complex inclusions, and silicates, were determined for the raw data. The Mn-Al-S field represents the MnS, Al_2O_3, and complex inclusions constituted by MnS and Al_2O_3. Based on the Al content, samples were split into three regions for classification: (1) Less than 30% Al for MnS inclusions, (2) Between 30 and 70% being complex inclusions of MnS and Al_2O_3 in an agglomerate, and (3) Greater than 70% Al being consistent with Al_2O_3. Other rules include greater than 10% Mn and S correlating with MnS and less than that being necessary to classify a particle as another phase. Silicates which are the primary phase in the Mn-S-Si phase were described as
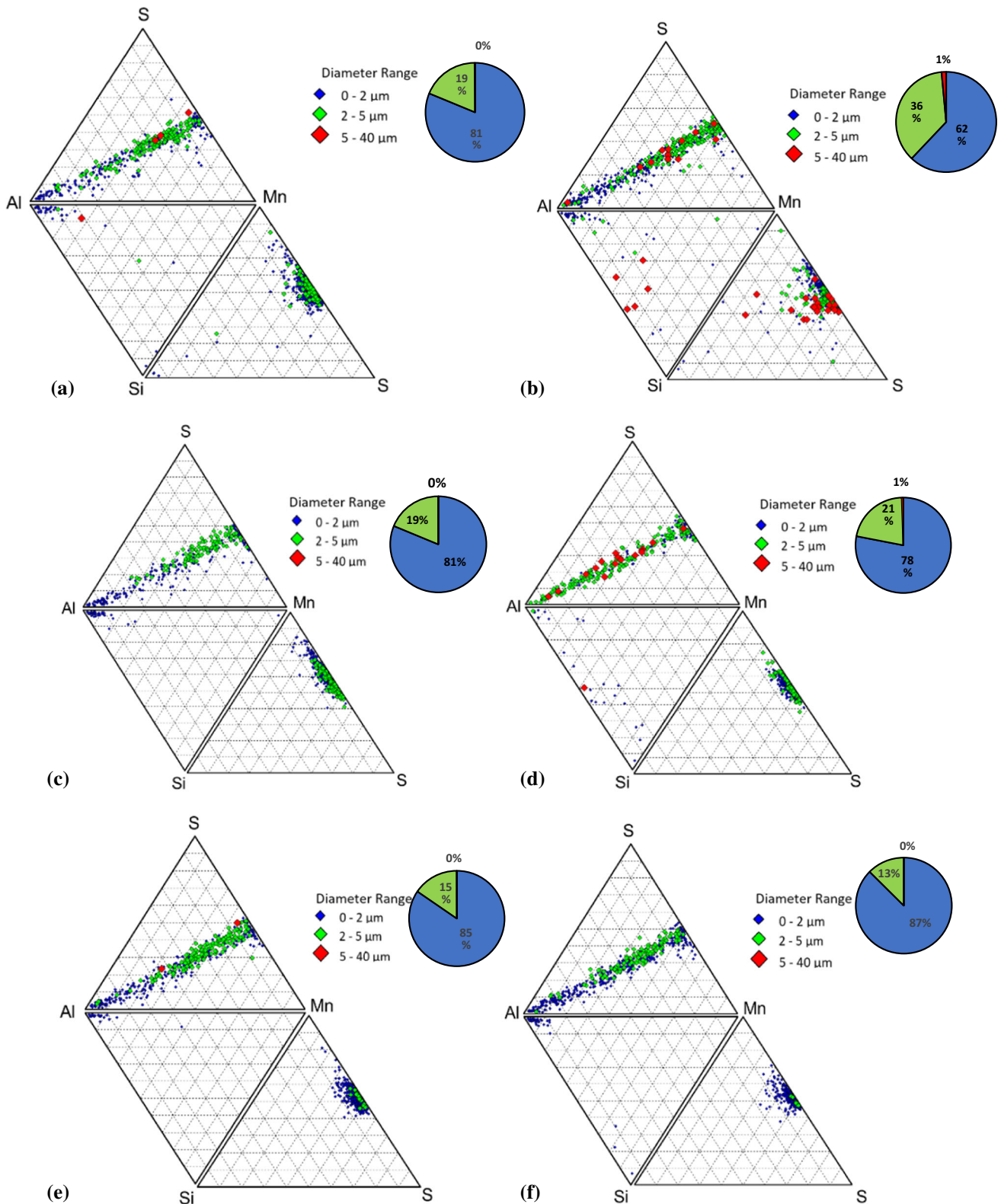
Figure 14. Ternary classification of the results from the Aspex AFA of the as-cast, as-rolled 830 and 1200 °C along with a pie chart of the overall NMI size (%) is depicted. The as-cast condition is shown in the L-S orientation (a) and T-L orientation; (b) as-rolled 830 °C is compared for the L-S orientation (c) and T-L orientation (d), and the as-rolled 1200 °C is compared for the L-S orientation (e) and T-L orientation (f). While it may seem insignificant, the 1% of particles >5 μm in the T-L orientation at 830 °C is the first indication of temperature dependence of NMI.
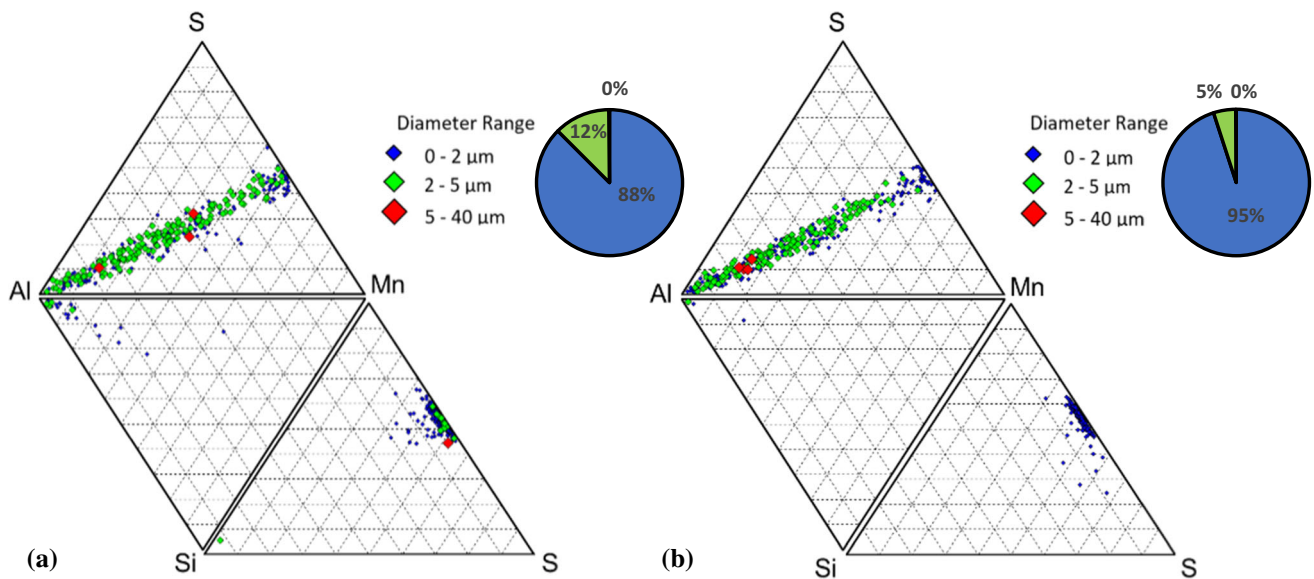
Figure 15. Ternary classification of the results from the Aspex AFA of the as-rolled conditions 900 (a) and 1000 °C (b) along with a pie chart of the overall NMI size (%) in the T-L direction.

Table 5. Summary of the Area Fraction in ppm of NMIs in Each Condition in the T-L Orientation

Condition (T-L)	Nonmetallic inclusions and porosity Amounts (ppm)					
	MnS	Al_2O_3	Complex	Silicates	Porosity	Total (ppm)
As-cast	466.2	14.4	30.7	38.2	225.6	775.0
As-rolled 830 °C	503.2	24.2	46.6	6.1	28.4	608.5
As-rolled 900 °C	337.4	22.0	42.9	0.3	56.6	459.3
As-rolled 1000 °C	215.1	27.6	43.3	0.0	38.2	324.2
As-rolled 1200 °C	373.4	15.4	25.7	0.0	2.6	417.1

Table 6. Summary of the Area Fraction in ppm of NMIs in Each Condition in the L-S Orientation

Condition (L-S)	Nonmetallic inclusions and porosity Amounts (ppm)					
	MnS	Al_2O_3	Complex	$CaAl_2O_4$	Porosity	Total (ppm)
As-cast	567.5	9.9	27.1	0.2	178.5	783.2
As-rolled 830 °C	836.1	13.8	27.7	11.8	11.8	891.3
As-rolled 1200 °C	515.7	29.2	40.1	7.3	7.3	604.1

having a Si content that exceeds 10% but less than 90% and a mixture of Al, Ca, and Mn that was between 30 and 90%. By characterizing the data in that manner, the area fraction of each NMI was determined for each condition and is represented in Table 5 for the T-L orientation and Table 6 for the L-S orientation with the shrinkage porosity content included from the previous section to represent the total steel cleanliness from the stitch scan. The expected result is that the overall content of combined steel cleanliness should be close to equivalent for all conditions since they are of the same heat and sample location. MnS content varied 7 to 35% from the average between samples. The

Al_2O_3 content varied 13 to 32% from the average, and complex inclusion content ranges from ~ 6 to 33% from the average for all samples. The biggest difference in the composition is the apparent mixed silicate of Mn and Al content in the T-L orientation and $CaAl_2O_4$ content in the L-S orientation. $CaAl_2O_4$ was excluded from the T-L table as the contents are quite small in all conditions, $\sim 0.003\%$, and the same was done for the L-S orientation with mixed silicates of Mn and Al. Table 7 lists the average alloy composition from the EDS measurements of the classified particles in the as-cast and as-rolled conditions which were averaged over all conditions with respect to the

Table 7. The Average Inclusion Compositions for Classified Particles Averaged for the As-Cast and As-Rolled Conditions Which Includes MnS, Al_2O_3, Complex Inclusions of MnS and Al_2O_3, Mixed Silicates, and $CaAl_2O_4$

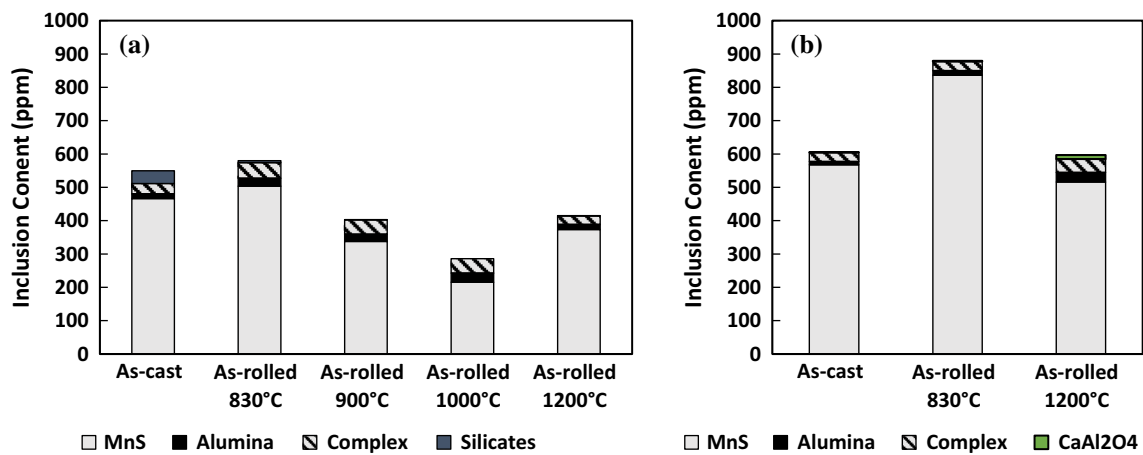| Inclusion classification	Average composition from EDS					
	Mg	Al	Si	S	Ca	Mn
MnS	0.0	0.5	0.4	46.1	0.0	52.9
Al_2O_3	1.3	91.6	0.9	2.1	0.5	3.6
Complex	0.7	49.5	0.5	22.4	0.3	26.6
Mixed Silicates	1.6	44.8	33.7	2.9	6.7	10.3
	Mg	Al	Si	S	Ca	Mn
MnS	0.0	0.6	0.6	45.2	0.1	53.6
Al_2O_3	1.1	91.2	1.2	1.5	1.5	3.6
Complex	0.5	46.1	0.6	23.4	0.3	29.2
$CaAl_2O_4$	0.1	82.0	1.9	0.4	13.4	2.2

Figure 16. A graphical representation of the area fraction of the NMIs in each condition for the T-L (a) and L-S (b) orientations.

individual orientations investigated which show good agreement.

The data are also represented graphically in Figure 16 for both the L-S orientation and T-L orientation. From Figure 16, it can be seen that MnS comprises the majority of the area fraction in both cases (75–95%) of each condition which is expected due to the Mn and S content of the steel. The majority of inclusions are endogenous. The small inclusions observed remain from steelmaking due to the inability to float to the slag layer prior to solidification. MnS forms preferentially on Al_2O_3 forming complex inclusions. While the variance in MnS content is unexpected, the variance between the majority of the samples is relatively low as they are all sampled from the same heat in the same location. The as-rolled 1000 °C is the only sample which shows evidence of significant decrease in the MnS.

The area fraction, number density, and aspect ratio for each major inclusion were investigated to determine if there is

an effect of hot rolling on NMI evolution. MnS inclusions are displayed for the L-S and T-L orientation in Figure 17. For the upper and lower temperatures which were investigated in the L-S orientation, the dependence on hot rolling temperature for area fraction (Figure 17a), number density (Figure 17c), and aspect ratio (Figure 17e) seems to be very little if any. The MnS have a similar area fraction and number density to that of the as-cast material in the L-S orientation. The T-L orientation, however, shows a shift in MnS size and area fraction, when investigating the differences in the MnS content in each sample it is evident that these peaks coincide with the MnS content. The aspect ratio of the as-rolled conditions shows an increase from the as-cast condition which shows some evidence that hot rolling has elongated them preferentially in the rolling direction which occurs due to the high deformability of MnS inclusions at hot working temperatures; however, the as-rolled condition at 830 °C seems to be the only sample with appreciable size as measured in the Aspex. In the L-S orientation, the Al_2O_3 inclusions shown in Figure 18 have a
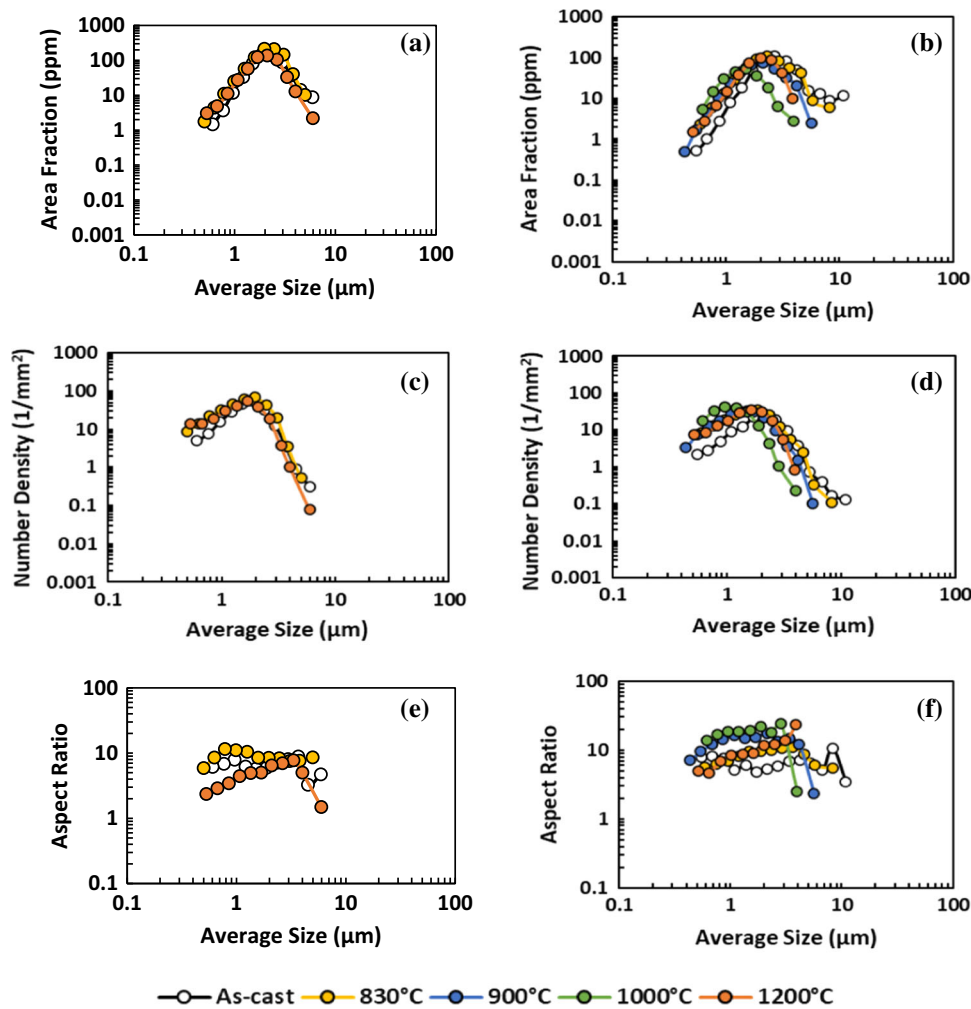
Figure 17. The average size, distribution, and morphology of MnS inclusions were examined from the Aspex PICA-1020 results. The as-cast, as-rolled 830 °C, and as-rolled 1200 °C were examined in the L-S orientation for area fraction (ppm) (a), number density (1/mm²) (c) and aspect ratio (e) vs. average size. The as-cast and as-rolled isothermal temperatures of 830, 900, 1000, and 1200 °C were also examined in the T-L orientation for area fraction (ppm) (b), number density (1/mm²) (d), and aspect ratio (f) vs. average size.

very similar size and distribution in the as-cast and as-rolled conditions (Figure 18a) which is also observable in the number density (Figure 18c). In the T-L orientation (Figure 18b), the slight decrease in overall area fraction of Al_2O_3 results in a decrease in the average size and density with the area fraction being similar for each condition. The complex inclusions are investigated in Figure 19. From Figure 19a, the area fraction of complex inclusions in the L-S orientation seems to increase slightly with rolling temperature. No appreciable difference should be noted in the complex inclusion population though with similar aspect ratios as well. The relationship in the T-L orientation shows that the area fraction distribution peak is increasing with decreasing temperature (Figure 19b). However, this shift is not appreciable, and even though there may be a slight differences in the inclusion population, other factors may be more influential on mechanical

properties. This is also supported by the low aspect ratio for all rolling conditions regardless of size which will not favor crack propagation along complex inclusions (Figure 19f).

The nearest-neighbor density (NND) averaged between all particles is displayed in Table 8. This includes the distance between MnS, Al_2O_3, complex, and silicate inclusions with 75 to 95% of the particles in each condition being constituted by MnS inclusions. The L-S orientation shows that the NND increases between the as-cast and as-rolled 830 °C from 6.9 to 9.4 μm and again from 830 to 1200 °C with an increase from 9.4 to 14.8 μm. In the T-L orientation, the spacing between particles is fairly similar between the as-cast sample and the material rolled at 830 and 1000 °C. However, 1200 °C is different showing a NND of 14.9 μm as opposed to 12.1 μm in the as-cast condition. This seems to further support the relationship in the L-S orientation.
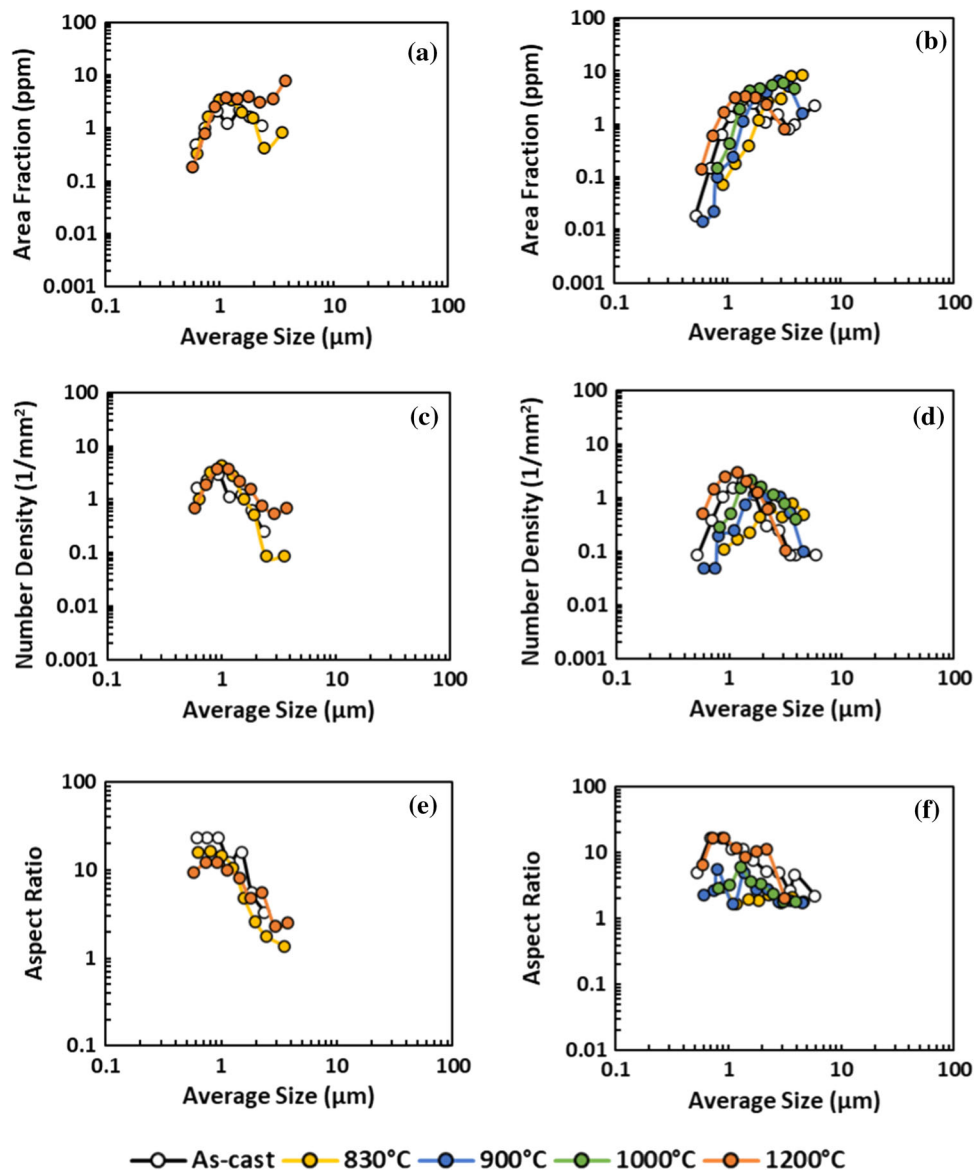
Figure 18. *The average size, distribution, and morphology of Al_2O_3 inclusions were examined from the Aspex PICA-1020 results. The as-cast, as-rolled 830 °C, and as-rolled 1200 °C were examined in the L-S orientation for area fraction (ppm) (a), number density ($1/mm^2$) c and aspect ratio (e) vs. average size. The as-cast and as-rolled isothermal temperatures of 830, 900, 1000, and 1200 °C were also examined in the T-L orientation for area fraction (ppm) (b), number density ($1/mm^2$) (d), and aspect ratio (f) vs. average size.*

An interesting relationship is that the NND increases from the L-S to T-L in the as-cast and as-rolled 830 °C but at 1200 °C is similar for both orientations. In general, an increase in the NND would be expected to be beneficial but the morphology of the inclusions can outweigh that relationship.

To verify the results of the automated analysis, the cross section of the fracture surface was prepared as described in Figure 5. BSE images of the fracture surface of the as-cast, as-rolled 830 °C, and as-rolled 1200 °C are displayed in Figure 20. These three specimens are selected to best

represent the temperature dependence of NMIs. More secondary cracking is observed in the as-cast material (Figure 20a); however, it is not related to NMI from the observed image although the T-L orientation will also be observed to further detail the cast structure. At 830 °C (Figure 20b), the MnS shows strong orientation dependence in the rolling direction. The MnS highlighted by the fracture surface is quite long ($\sim$190 µm), which further highlights the relationship with increased MnS content and more detrimental morphology in the 830 °C sample. In comparison, the MnS at 1200 °C still shows orientation dependence in the rolling direction but is finer in
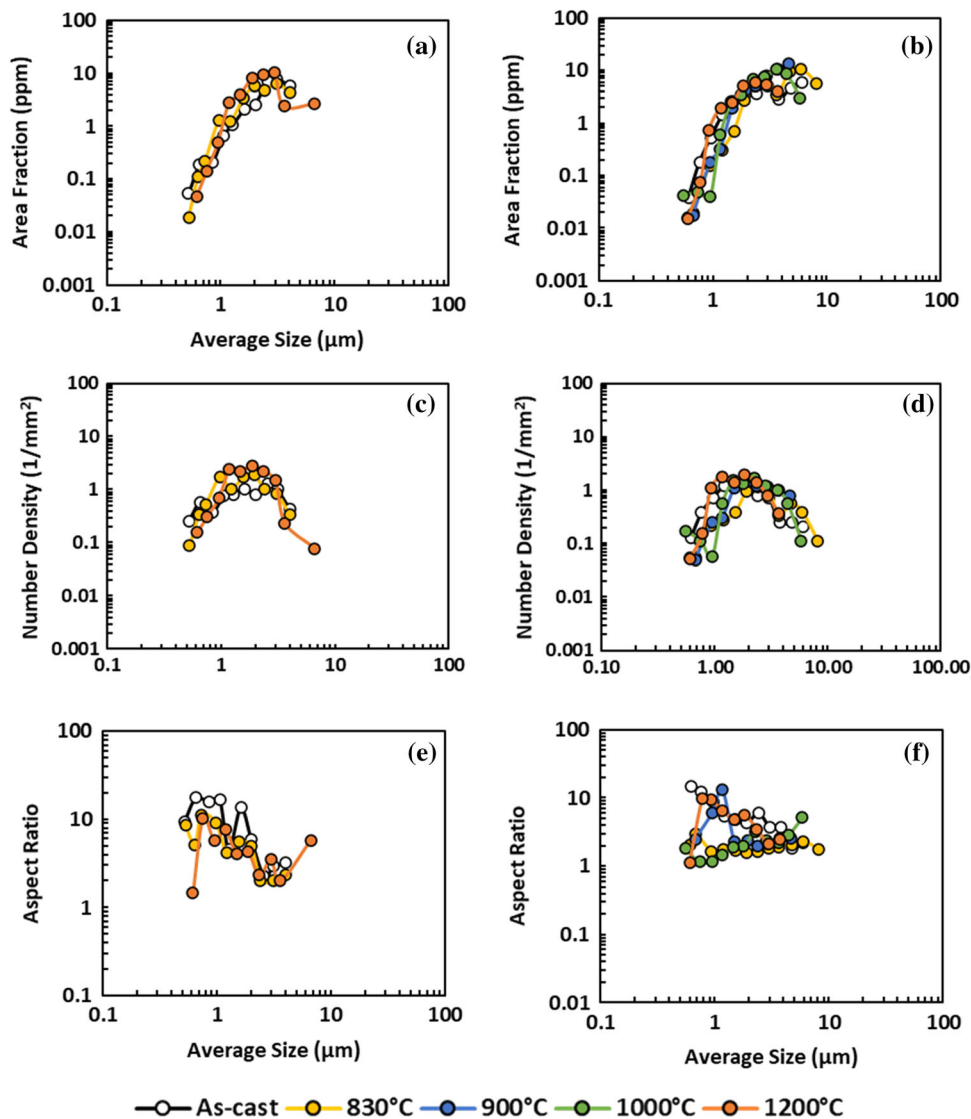
Figure 19. The average size, distribution, and morphology of complex inclusions were examined from the Aspex PICA-1020 results on log-log plots. The as-cast, as-rolled 830 °C and as-rolled 1200 °C were examined in the L-S orientation for area fraction (ppm) (a), number density (1/mm²) (c) and aspect ratio (e) vs. average size. The as-cast and as-rolled isothermal temperatures of 830, 900, 1000, and 1200 °C were also examined in the T-L orientation for area fraction (ppm) (b), number density (1/mm²) (d), and aspect ratio (f) vs. average size.

comparison with the 830 °C condition explained by a decrease in the MnS content. It is possible that the MnS morphology and anisotropy ratio are linked. However, the similar behavior at 830 and 900 and 1000 and 1200 °C may indicate that recrystallization and texture also play a role. Higher-magnification images were also taken in the cross section of the L-S orientation which show the interaction between MnS inclusions and secondary cracking in the as-rolled 900 °C and as-rolled 1000 °C which both show evidence of initiation and propagation as a result of MnS inclusions.

At 900 °C (Figure 21a), inclusions were examined with energy-dispersive spectroscopy (EDS) to verify their

composition which were verified to be MnS inclusions. The secondary crack initiates at the first MnS inclusion near the fracture and propagates through the matrix transgranularly until it reaches the second MnS. The secondary crack distorts the 2nd MnS but propagation does not continue; however, the secondary cracking is perpendicular to the primary crack direction which indicates the strain induced by the MnS making it preferable for crack propagation. At 1000 °C (Figure 21b), a smaller overall Type II MnS is observed; however, it has a detrimental morphology which leads to secondary crack initiation and propagation, verified through EDS. The cross section below the T-L fracture surface was also prepared as shown in Figure 22a. The as-cast (Figure 22a) and as-rolled 1200 °C (Figure 22b) show

Table 8. Average Nearest-Neighbor Distance (μm) in Each Condition

Condition	Average NND (μm)	Standard deviation (μm)
Longitudinal-Short orientation (L-S)		
As-cast	6.9	19.4
As-rolled 830 °C	9.4	17.0
As-rolled 1200 °C	14.8	22.1
Transverse-Longitudinal orientation (T-L)		
As-cast	12.1	29.6
As-rolled 830 °C	12.7	25.9
As-rolled 900 °C	13.7	26.9
As-rolled 1000 °C	12.1	22.4
As-rolled 1200 °C	14.9	25.3

different relationships with MnS inclusions. The as-cast material shows a void that seems to have initiated as a result of a Type II MnS inclusions and Al_2O_3 inclusions verified through EDS measurements. The as-rolled 1200 °C shows the morphology of MnS inclusions which seems to have split by particle decohesion of the particle matrix. This is in line with the literature regarding void sheet coalescence [9].

To correlate the Aspex PICA-1020 results to the Charpy impact results in previously published work, the projected length was determined using the number of plastic inclusions per unit area of the transverse-longitudinal specimens, or the longitudinal plane and the diameter of the inclusion parallel to the longitudinal plane. The following relationship (Eqn. 1) has been shown in literature to correlate to Charpy impact toughness for a low C steel:

$$P_2 = N_{A_3} * d_1 \qquad \text{Eqn. 1}$$

where N_{A_3} is defined as the number of plastic inclusions per unit area of the transverse longitudinal specimen, d_1 is the average diameter of the inclusion dimension parallel to the longitudinal direction, and P_2 is the projected length. The projected length was calculated from the Aspex PICA-1020 maximum diameter of MnS, assumed to be parallel to the longitudinal plane, and the number density of MnS inclusions (number of inclusions in the observed area). Plotting the average Charpy impact toughness for each isothermal rolling condition at a 66% cumulative reduction versus the projected length, a regression analysis was performed as shown in Figure 23. This relationship indicated that there is a relationship between projected length and average Charpy impact toughness in the transverse longitudinal specimens. An R^2 value of 0.730 indicates that the fit shows a trend but may not be suitable for direct predictions of Charpy impact toughness in the transverse-longitudinal orientation based on

projected length. However, an important result of this finding is that the area fraction of MnS was correlated to shifts in average inclusion diameter of MnS in Figure 18. Therefore, if there is a relationship between the projected length (a function of inclusion diameter) and number density (number of inclusions per unit area), the steel cleanliness, or more succinctly, S content should be inversely proportional to impact toughness in the T-L orientation. Therefore, careful monitor of steelmaking processes to limit the S content can reduce the anisotropy experienced in the 830 and 900 °C specimens.

Conclusions

By examining the results of the automated feature analysis at all temperatures and comparing to nearest-neighbor distance, temperature dependence on porosity closure was evident. The trend between 830 and 900 °C in terms of pores greater than 5 μm further indicated the drawbacks of the AFA as the expected trend in terms of nearest-neighbor distance would indicate that the region analyzed at 830 °C may have been "artificially clean" on the analyzed surface and the sample at 900 °C may have been more representative for the given temperature. Temperature dependence on coarse shrinkage porosity closure was observed from 900 to 1200 °C with 35 ppm decreasing to 1 ppm. The NND measurements further verified this relationship by indicating an increase in NND from 219 μm in the as-cast to 1246 in the as-rolled 1200 °C condition. While the resolution of the CT scan limited the correlation between the AFA and CT scan results, it was observed that ∼98% of shrinkage porosity in the as-cast condition with a mean diameter greater than 15.73 μm was closed for a 66% reduction at 1000 °C; the automated feature analysis extended the analysis to micro-voids down to 0.5 μm indicating that ∼92% of the total porosity was closed at 1000 °C. Area fraction, number density, and aspect ratio were investigated for relationship with rolling condition. MnS inclusion diameter seemed to be strongly correlated with area fraction of MnS. The aspect ratio also increased proportionally with MnS content during hot rolling resulting in longer MnS stringers in the as-rolled 830 °C condition. Al_2O_3 had a similar composition in each sample and showed little deviation in size and distribution. Complex inclusions of MnS and Al_2O_3 displayed a dependence of aspect ratio on the area fraction of the inclusions but were inversely proportional. Cross sections of the fracture surfaces revealed interactions between MnS inclusions and secondary cracking showing that elongated MnS inclusions initiated secondary cracks in the T-L orientation. The Type II MnS morphology was also seen to cause failure in the as-cast condition. Lastly, the projected length was compared to that of the average Charpy toughness for the T-L orientation and a correlation was observed indicating that projected length of MnS inclusions can be utilized to predict the impact toughness in the T-L orientation.
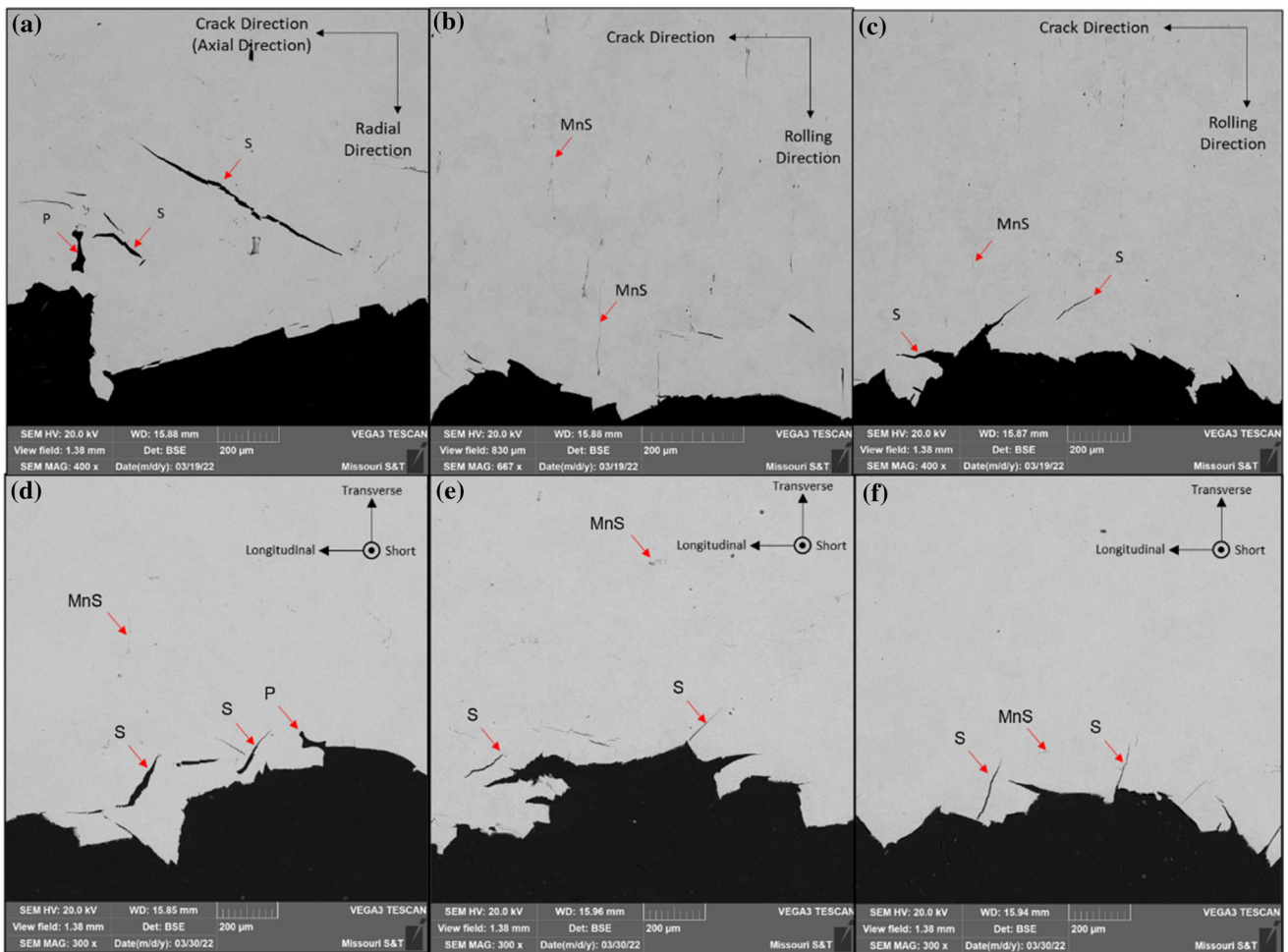
Figure 20. BSE images of a cross section of the fracture surface as depicted in Figure 5. The as-cast (a, d) includes "S" and "P" representing secondary cracks and shrinkage pore. The as-rolled 830 °C (b, e) includes "MnS" inclusions which can be seen elongated in the rolling direction. The as-rolled 1200 °C (c, f) includes "MnS" inclusions and "S" secondary cracks with elongated Type II MnS seen in the rolling direction but more fine than at 830 °C.
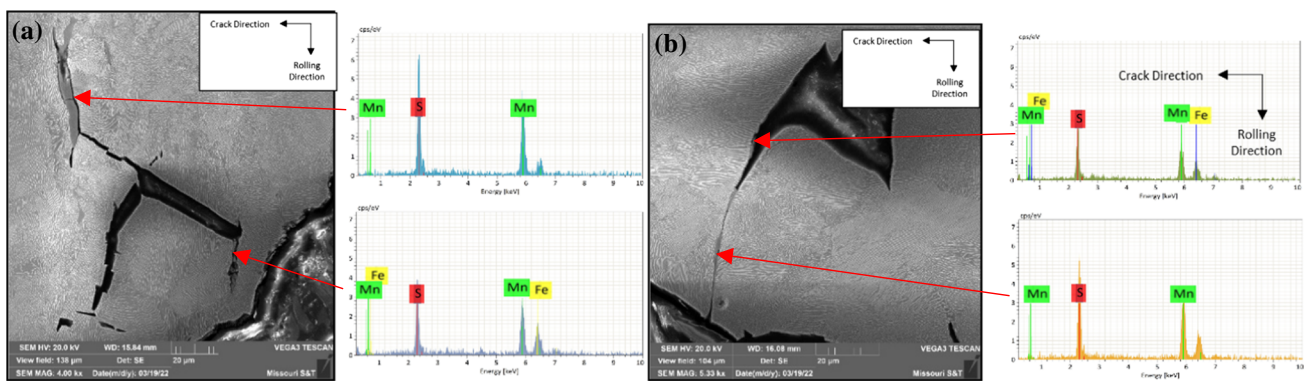

Figure 21. SE images of Type II MnS interaction with secondary cracks. As-rolled 900 °C (a) shows initiation of a secondary crack through Type II MnS which propagates transgranularly to a second MnS which cracks and debonds. As-rolled 1000 °C (b) shows initiation from Type II MnS at a slightly higher rolling temperature. Of note, no evidence was observed of MnS interaction at 1200 °C for the given sample.
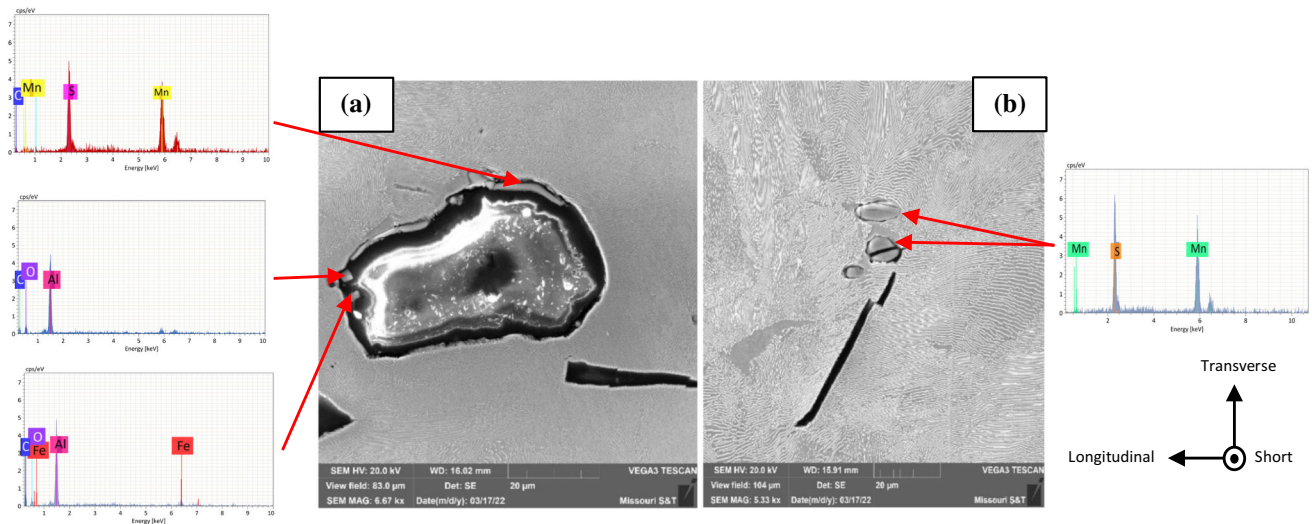
Figure 22. *SE images of Type II MnS interaction with secondary cracks in the T-L bars. The as-cast T-L bar (a) shows a large void with interaction of Type II MnS and Al2O3 which appear to be preferentially oriented on grain boundaries, leading to the failure. As-rolled 1200 °C (b) is depicted with secondary cracking leading to a MnS inclusion that has debonded and cracked from the stress of cracking. With respect to the orientation depicted the secondary cracking does not continue perpendicular to the crack direction as it initiated and traveled prior to interacting with the MnS.*
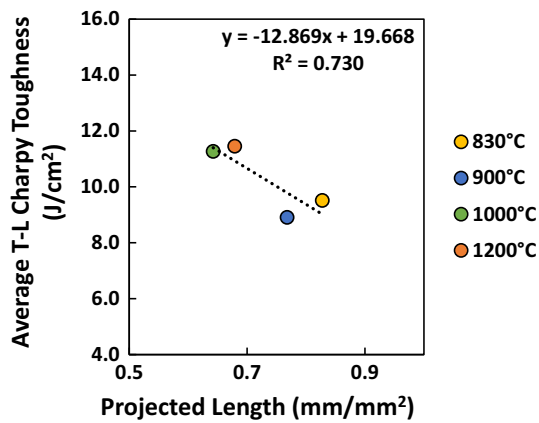
Figure 23. *Average transverse-longitudinal charpy toughness in J/cm^2 versus Projected length in mm/mm^2 indicating that there is a relationship between the projected length of plastic inclusions during hot rolling and impact toughness in the T-L orientation. "Plastic inclusions" are limited to MnS and the d_1 is assumed to be satisfied by the average maximum dimension in the longitudinal plane. The R^2 is 0.730 and therefore should not be used in place of similar measurement for other materials but does indicate a relationship is present which is in agreement with the work by Spitzig[9,10].*

Acknowledgements

Appendix 1

The volume in μm^3 versus mean diameter in μm is depicted in Figure 24 with regression analyses performed to predict their relationship. The regression formulas are represented in Eqn. 2 with a R^2=0.787 for the as-cast condition and Eqn. 3 with a R^2=0.954 for the as-rolled 1000 °C. With "y" representing the pore volume in μm^3 and "x" representing pore diameter in μm, Eqn. 2 was applied to the as-cast AFA results and Eqn. 3 was applied to the as-rolled 1000 °C AFA results to approximate the volume of the pores in the flat cross section.

$$y = 7.607x^{2.345} \qquad \text{Eqn. 2}$$

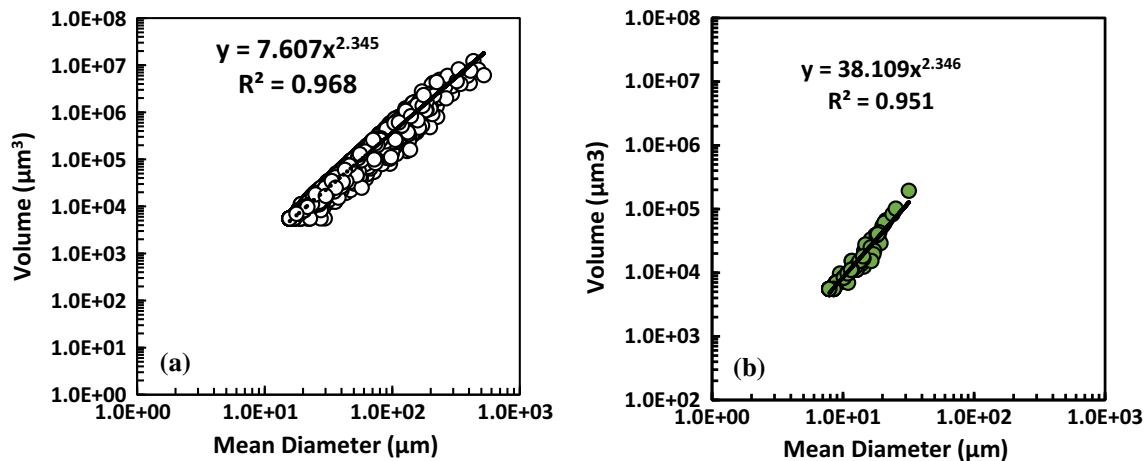$$y = 38.109x^{2.346} \qquad \text{Eqn. 3}$$

Figure 24. By plotting the mean diameter and volume of each pore from the 3D Objects Counter in Fiji for the central slice (3.2 mm height) a linear regression was fit to allow predictions of volume based on diameter.

REFERENCES

1. Rail Steels- Developments , Processing , and Use A Symposium. (2020).
2. R.A. Hardin, C. Beckermann, Effect of porosity on the stiffness of cast steel. Metall. Mater. Trans. A: Phys. Metall. Mater. Sci. **38**(12), 2992–3006 (2007). https://doi.org/10.1007/s11661-007-9390-4
3. A. Wang, P.F. Thomson, P.D. Hodgson, A study of pore closure and welding in hot rolling process. J. Mater. Process. Technol. **60**(1–4), 95–102 (1996). https://doi.org/10.1016/0924-0136(96)02313-8
4. S. Ganguly, X. Wang, K. Chandrashekhara, M.F. Buchely, S. Lekakh, R.J. O'Malley, D. Bai, Y. Wang, Modeling and simulation of void closure during Steckel mill rolling for steel plate. Steel Res. Int. **92**(2), 1–12 (2021). https://doi.org/10.1002/srin.202000293
5. M. Kukuryk, Experimental and FEM analysis of void closure in the hot cogging process of tool steel. Metals **9**(5), 538 (2019). https://doi.org/10.3390/met9050538
6. S. Dhua, A. Ray, S.K. Sen, M.S. Prasad, K.B. Mishra, S. Jha, Influence of nonmetallic inclusion characteristics on the mechanical properties of rail steel. J. Allergy Clinical. Immunol. **130**(2), 556 (1998). https://doi.org/10.1016/j.jaci.2012.05.050
7. K.V. Grigorovich, A.S. Trushnikova, A.M. Arsenkin, S.S. Shibaev, A.K. Garber, Structure and metallurgical quality of rail steels produced by various manufacturers. Russian Metall. (Metally) **2006**(5), 427–438 (2006). https://doi.org/10.1134/S0036029506050107
8. D. Douglas, C.V. White, T. McHenry, Failures related to hot forming processes, in *Analysis and prevention of component and equipment failures*. ed. by B.A. Miller, R.J. Shipley, R.J. Parrington, D.P. Dennies (ASM International, UK, 2021), pp.229–240. https://doi.org/10.31399/asm.hb.v11a.a0006835
9. W.A. Spitzig, Effect of sulfides and sulfide morphology on anisotropy of tensile ductility and toughness of Hot-ROLLED C-Mn steels. Metall. Trans. A, Phys. Metall. Mater. Sci. **14**(2), 471–484 (1983). https://doi.org/10.1007/bf02644224
10. E. Da Costa, A.L.V. Silva, The effects of non-metallic inclusions on properties relevant to the performance of steel in structural and mechanical applications. J. Market. Res. **8**(2), 2408–2422 (2019). https://doi.org/10.1016/j.jmrt.2019.01.009
11. J.J. Moore, G. Bodor, Steel deoxidation practice: Special emphasis on heavy section steel castings. AFS Trans. **93**, 99–114 (1985)
12. Singh V, Lekakh S, Peaslee K (2008). Using automated inclusion analysis for casting process improvements. In: SFSA technical and operating conference, Steel Founders' Society of America (SFSA), May, 1–18. http://scholarsmine.mst.edu/post_prints/pdf/TO_08_MSTInclusions_09007dcc805d93e9
13. Y. Tanaka, F. Pahlevani, V. Sahajwalla, Agglomeration behavior of non-metallic particles on the surface of Ca-treated high-carbon liquid steel: an in situ investigation. Metals **8**(3), 176 (2018). https://doi.org/10.3390/met8030176